Title	Computation of Self-Induced Magnetic Field Effects Including the Lorentz Force for Fast-Transient Phenomena in Integrated-Circuit Devices
Author(s)	Schoenmaker, W; Chen, Q; Galy, P
Citation	IEEE Transactions on Computer-Aided Design of Integrated Circuits and Systems, 2014, v. 33, p. 893-902
Issued Date	2014
URL	http://hdl.handle.net/10722/200614
Rights	Creative Commons: Attribution 3.0 Hong Kong License

Computation of Self-Induced Magnetic Field Effects Including the Lorentz Force for Fast-Transient Phenomena in Integrated-Circuit Devices

Wim Schoenmaker, Quan Chen, *Member, IEEE,* and Philippe Galy

Abstract—We present a full physical simulation picture of the electromagnetic phenomena combining electromagnetic (EM) fields and carrier transport in semiconductor devices (TCAD) in the transient regime. The simulation tool computes the EM fields in a self-consistent way and the resulting magnetic fields are incorporated in the computation of the current sources that get modified by the Lorentz force (LF).

Index Terms—Electromagnetics, Lorentz force (LF), TCAD, Transient.

I. INTRODUCTION

THE SINGLED-out purpose of electrostatic discharge (ESD) devices is that these devices should protect electronic circuitry against fast-transient voltage/current spikes. Although the overall signal variation occurs within a nanosecond, the corresponding currents can ramp up to multiampere levels. Fast varying current patterns give rise to equally fast varying induced magnetic fields, being proportional to the rate of change of the current. As a consequence, a substantial part of the electric fields can be attributed to the variation of the induced magnetic fields and the full electromagnetic picture is required for understanding the effects of fast-transient input signals. A similar reasoning can be done for high-power switch devices. Continuing the reasoning along these lines, when the fields are varying sufficiently fast, both the induced magnetic fields and electric fields will ultimately have such large components such that the current flow is controlled by both fields. In particular, in semiconductors, the Hall coefficient is directly related to the carrier mobility and therefore self-induced Lorentz force (LF) modifications could become appreciable. So far, no simulation tool has

W. Schoenmaker is with Magwel NV, B-3600 Leuven, Belgium (e-mail: wim.schoenmaker@magwel.com).

Q. Chen is with the Department of Electrical and Electronic Engineering, University of Hong Kong, Kowloon, Hong Kong (e-mail: quanchen@eee.hku.hk).

P. Galy is with STMicrolectronics Research and Development, 38926 Crolles, France (e-mail: philippe.galy@st.com).

been designed to address these concerns and strictly speaking, without actually computing these effects, we have no clue if it is justified to ignore these subtleties altogether or that these effects are really a concern. The purpose of the present work is to fill this gap. We present an implementation that allows the computation of these self-induced electromagnetic field effects for fast transient phenomena. In particular, the key ingredients are: 1) the semiconductor device equations; 2) modifications thereof to account for the LF; and 3) the Maxwell's equations to compute the electromagnetic (EM) fields. All this is done in the time domain, since in the frequency domain the small-signal analysis upfront excludes high current/voltage signals at the ports. In the remainder of the paper, we refer to the Maxwell's equations with electromagnetism (EM) and to the semiconductor equations with drift-diffusion model (DD). Finally, the modifications are induced by the LF. The EM-TCAD simulation refers to a concurrent solution of the Maxwell's equations that describe the EM dynamics and the transport models that describe the charge carrier dynamics in semiconductor devices. So far, only a few frameworks have been developed to allow such coupling, see [1]–[3], based on different selections of EM and TCAD solvers. One experimentally verified cosimulation framework was first proposed in [4] and [5] in the frequency domain. The Maxwell's equations are formulated in terms of the scalar potential *V* and vector potential **A** to obtain straightforward coupling with the DD semiconductor model (called the A-V formulation henceforth). The spatial discretization scheme based on the finite-volume method (FVM) and finite-surface method (FSM) is fully compliant with the geometric meaning of the differential operators. The motivation for selecting the FVM is found in the desire to connect the field solver results directly to the variables that are commonly used in the electronic design environment, i.e., currents and voltages. In other words, the voltages (V) at the contacts are in one-to-one correspondence with node voltages at a SPICE net list and the currents entering/leaving the circuit fragment simulated by a field solver are in one-to-one correspondence with the end point(s) of some net list branch(es). A convenient link is established between the field solver and Kirchhoff's voltage and current laws. Successful simulations of semiconductor devices always have exploited charge conservation as an essential ingredient of the modeling that could be achieved using the FVM. It is noted that the FVM is mimetic [6] and

relaxes the demand that for finite grid sizes, every variable should be calculable at every space–time point. In other words, only in the limit of zero grid-node distance ($\lim h \to 0$) such detailed information may be extracted. For example, the finite-integration method [7], which belongs to the class of FVM, puts the electric field on the links of the grid and the magnetic field on the surfaces of the grid. No statement is made about these fields for space points that are neither on the links or surfaces. The benefit is that the geometrical character of the field variables are faithfully implemented and the constraints are obeyed without additional effort. Finally, the conservation of charge is built-in from the start.

In addition to these practical advantages, the FVM can be justified from Noether's theorem [8] which states that to every conserved quantity there corresponds an invariance principle. Strictly speaking, the relation is reverse, i.e., to every invariance principle there corresponds a conserved quantity. Thus in order to respect charge conservation, we must build in the underlying invariance principle. For the electromagnetic fields, the invariance is realized for the scalar potential and the vector potential that may be transformed without altering the physical content. Accepting voltages (V) as degrees of freedom in the modeling set up requires that for the inclusion of magnetic effects, the vector potential (**A**) must be also part of the set of degrees of freedom.

A time-domain A–V simulator has been proposed in [9] and [10] to meet the desire to handle the large-signal response and to complement the small-signal analysis applied in its frequency-domain counterpart. The implicit backward Euler (BE) approach was employed for time discretization, and the Newton's method was used to solve the nonlinear system that arises from the semiconductor dynamics. Whereas [10] deals with field transformations to capture ultrafast time variations, this paper does not exploit these transformations but aims to include the LF. Due to the extended physical reality and its numerical treatment, five variables are used and solved simultaneously in the formulation. Three variables are located on nodes and two variables are defined on links. Therefore, the number of unknowns in each Newton iteration can be ~ 9 times the number of nodes in the computational grid for large-scale problems. The discretization of the LF impact on currents was addressed in [11] and [12]. The emphasis of this paper was on finding a proper discretization of higher order field expressions such as $\mathbf{E} \times \mathbf{B}$. Again, the current balance is a key guideline in the discretization procedure, and the mimetic methods that respect the geometrical meaning of the various observables are capable of arriving at very accurate results. In particular, comparing the outcome of the numerical approach with analytic results (for the rare case where such results can be found) demonstrates that the proposed discretization method is very reliable. Although it was anticipated in [11] and [12] that the self-induced LF will become only important, if it will be at all, in fast-transient regimes, the paper in [11] and [12] is limited to the static regime. In this paper, we will report about the full transient implementation of the proposed methods. This brings us to the following organization of this paper. Section II reviews the A–V formulation of EM-TCAD problem and the conventional solution scheme.

Section III describes the extension to include the Lorentz force. In Section IV, we address the discretization of the Lorentz force as well as the numerical subtleties that are encountered when solving the full EM-TCAD-LF problem. Numerical experiments that verify the proposed approach are presented in Section V. Conclusions are presented in Section VI.

II. TIME-DOMAIN FORMULATION OF EM-TCAD PROBLEM

The starting point of the time-domain EM-TCAD formulation is the full-wave Maxwell's equations

$$\nabla \cdot \mathbf{D} = \rho, \quad \nabla \cdot \mathbf{B} = 0 \tag{1a}$$

$$\nabla \times \mathbf{E} = -\partial_t \mathbf{B}, \quad \nabla \times \mathbf{H} = \mathbf{J} + \partial_t \mathbf{D} \tag{1b}$$

$$\mathbf{D} = \epsilon \mathbf{E}, \quad \mathbf{B} = \mu \mathbf{H} \tag{1c}$$

where **D**, **E**, **B**, **H**, **J**, and ρ are the displacement field, electric field, magnetic induction, magnetic field, free current density, and charge density, respectively.

In the semiconductor region, the Maxwell's equations are complemented with the current-continuity of electrons and holes

$$\frac{1}{q}\nabla \cdot \mathbf{J}_n - \partial_t n - R(n, p) = 0 \tag{2a}$$

$$\frac{1}{q}\nabla \cdot \mathbf{J}_p + \partial_t p + R(n, p) = 0 \tag{2b}$$

where n and p are the electron and hole densities, and $R(n, p)$ denotes the net generation/recombination rate of carriers and q is the elementary charge. The particle current densities in semiconductor are described by the DD model

$$\mathbf{J}_n = q\mu_n n\mathbf{E} + kT\mu_n \nabla n \tag{3a}$$

$$\mathbf{J}_p = q\mu_p p\mathbf{E} - kT\mu_p \nabla p \tag{3b}$$

where ϵ is the permittivity, μ is the magnetic permeability, μ_p, μ_n, k, and T denote the carrier mobilities, Boltzmann constant, and temperature, respectively.

To facilitate the coupling between the EM and TCAD solvers, the Maxwell's equations are written in potential form using the variables V and **A** with the result that $\mathbf{B} = \nabla \times \mathbf{A}$ and $\mathbf{E} = -\nabla V - \partial_t \mathbf{A}$ [4], [5]. A new variable, the pseudo-canonical momentum

$$\Pi = \partial_t \mathbf{A} \tag{4}$$

is also introduced to avoid the second-order time derivative [9]. The complete system of equations is then laid out in (5) utilizing a generalized de Mari scaling scheme [5], [10]

$$\begin{cases} \frac{1}{v}\nabla \cdot [\varepsilon_r(-\nabla V - \Pi)] - \rho = 0, \quad \rho = p - n + N_D \\ \frac{1}{v}\nabla \cdot [\varepsilon_r(-\nabla \partial_t V - \partial_t \Pi)] + \begin{cases} \nabla \cdot [\sigma(-\nabla V - \Pi)] & \text{metal} \\ \nabla \cdot \mathbf{J}_{sd} & \text{semi/metal} \end{cases} \\ = 0 \end{cases}$$
$$\tag{5a}$$

$$\nabla \cdot \mathbf{J}_n - \partial_t n - R(n, p) = 0 \tag{5b}$$

$$\nabla \cdot \mathbf{J}_p + \partial_t p + R(n, p) = 0 \tag{5c}$$

$$\partial_t \mathbf{A} - \Pi = 0 \tag{5d}$$

$$- K\varepsilon_r \left(-\partial_t \Pi - \nabla \partial_t V\right) - K\nabla \left(\varepsilon_r \partial_t V\right)$$
$$+ \left[\nabla \times (\nabla \times \mathbf{A}) - \nabla (\nabla \cdot \mathbf{A})\right]$$
$$- K\nu \left\{ \begin{array}{ll} \mathbf{J}_\mathrm{c} & \text{metal} \\ \mathbf{J}_\mathrm{sd} & \text{semi} \end{array} \right\} = 0 \quad (5e)$$

where $\mathbf{J}_\mathrm{c}$ is the conduction current in metal and $\mathbf{J}_\mathrm{sd} = \mathbf{J}_\mathrm{n} + \mathbf{J}_\mathrm{p}$ is the total semiconductor current (see Section III). K and ν are two dimensionless constants of the scaling method [10]. In the scaling scenario where λ_L and λ_T are the natural units of length and time, we find that $K = \mu_0 \epsilon_0 \lambda_\mathrm{L}^2 / \lambda_\mathrm{T}^2$. For example, for a small-size microelectronic device with a typical length of about one micrometer and a switching frequency around 5 GHz, we may set $\lambda_\mathrm{L} = 10^{-6}$ m and $\lambda_\mathrm{T} = 10^{-10}$ s. The dimensionless parameter ν corresponds to the characteristic relaxation time of conductive materials. In particular, if λ_COND is the 'natural unit' of conductance (for example $\lambda_\mathrm{COND} = 10^7$ S/m for Aluminum) we find that $\nu = \lambda_\mathrm{COND} \times \lambda_\mathrm{T} / \epsilon_0$. The meaning of the parameter ν becomes clear when combining Gauss' law with the current-continuity and eliminating the electric field, i.e., $\frac{\sigma}{\epsilon} \rho + \partial_t \rho = 0$ or $\rho \sim \exp \left(-\frac{\sigma t}{\epsilon}\right)$. We also note that natural units can be chosen within a range of applicability. In other words, an equally valid choice is $\lambda_\mathrm{L} = 10^{-5}$ m or $\lambda_\mathrm{L} = 10^{-7}$ m in the above discussion. An unnatural choice would be to describe the microelectronic devices using 1 km as a basis for expressing lengths. The scaling of the system can be further improved by using quasi-Fermi potentials, ϕ^p and ϕ^n. The relation is

$$n = n_i \exp \left(\frac{q}{kT}(V - \phi^\mathrm{n})\right) , \quad p = n_i \exp \left(\frac{q}{kT}(\phi^\mathrm{p} - V)\right) \quad (6)$$

and by scaling the semiconductor current-continuity equations with the nodal carrier densities. Equation in (5a) is the common Gauss' law, and (5e) is the current-continuity equation that is applied to nodes for which there is attached at least one grid cell consisting of a conductor (metal). For these nodes, Gauss' law is used to recover the charge densities which are not explicit unknowns. Note that a node may be located at a metal/insulator or metal/semiconductor or a metal/semiconductor/insulatior (triple point) interface. As a consequence, the discretization or equation assembling receives contribution from both metallic and semiconductor cells. Therefore, both current types are found in (5a). The scaled current-continuity equations are given in (5b) and (5c) whereas (5d), equal in appearance as (4) is the scaled version of the pseudo-canonical momentum definition. The Maxwell–Ampere equation is given in (5e). It includes the subtraction of the divergence of Lorentz gauge condition

$$\nabla \cdot \mathbf{A} + K\varepsilon_r \partial_t V = 0 \quad (7)$$

to eliminate the intrinsic singularity of the curl–curl operator [13] and obtaining a Laplacian-like operator $\nabla^2 = \nabla(\nabla \cdot) - \nabla \times (\nabla \times)$. The numerical subtleties in the various transient regimes have been addressed in [10]. In particular, the fact that the $A - -V$-formulation ultimately breaks down if the transient times get too small (10^{-14} s). However, it is assumed that for such short time signals the DD model becomes questionable [14] and the relevance of the full EM-TCAD setup is at stake. Therefore, we limit the fast-transient signals in a range of $O(10^{-14}) - O(10^{-9})$ seconds.

III. INCLUSION OF THE LORENTZ FORCE

In this section, we will present the equations that will serve as a starting point for the implementation of the Hall effect and the self-induced Lorentz forces (LFs). First of all, we emphasize that the LF, although having a magnetic origin, is not related to skin effects and proximity effects. The latter correspond to altering the current flow due to the presence of time-varying magnetic fields, thereby altering the electric field. The currents are related to the electric field according to Ohm's law in metallic domains and according to the drift-diffusion current-continuity equations in semiconducting domains. However, the Lorentz force impacts Ohm's law and the DD model itself. The starting point of the discussion of the LF is the well-known LF law

$$\mathbf{F}(t) = q\mathbf{E}(t) + q\mathbf{v}(t) \times \mathbf{B}(t). \quad (8)$$

This force can be inserted into the Boltzmann transport equation that requires the description of external forces applied to the point particles moving in configuration space and by adapting the moment expansion, the upgraded equations of Ohm's law and the DD model are obtained. In metallic regimes, one finds

$$\mathbf{J}(t) = \sigma\mathbf{E}(t) + \mu_\mathrm{H}\mathbf{J}(t) \times \mathbf{B}(t) \quad (9)$$

where μ_H is the Hall coefficient.[1] In order to keep track of the transient modifications, we explicitly denote the time dependence. In semiconducting regions, the current densities for holes and electrons in the DD model with inclusion of the LF are

$$\begin{aligned} \mathbf{J}_\mathrm{n}(t) &= q\mu_\mathrm{n}n(t)\left(\mathbf{E}(t) + \mathbf{v}_\mathrm{n}(t) \times \mathbf{B}(t)\right) + kT\mu_\mathrm{n}\nabla n(t) \\ \mathbf{J}_\mathrm{p}(t) &= q\mu_\mathrm{p}p(t)\left(\mathbf{E}(t) + \mathbf{v}_\mathrm{p}(t) \times \mathbf{B}(t)\right) - kT\mu_\mathrm{p}\nabla p(t) \end{aligned} \quad (10)$$

where $\mathbf{J}_\mathrm{n}(t) = -qn(t)\mathbf{v}_\mathrm{n}(t)$ and $\mathbf{J}_\mathrm{p}(t) = qp(t)\mathbf{v}_\mathrm{p}(t)$ are implicitly defining the mean carrier velocities. The latter can be eliminated in favor of the current densities, and both equations can be expressed as [15]

$$\mathbf{J}_\mathrm{c}(t) + s\mu_c\mathbf{B}(t) \times \mathbf{J}_\mathrm{c}(t) = \mathbf{K}_\mathrm{c}^\mathrm{DD}(t). \quad (11)$$
$$\mathbf{K}_\mathrm{c}^\mathrm{DD}(t) = q\mu_c c(t)\mathbf{E(t)} - skT\mu_c\nabla c(t). \quad (12)$$

Here, $c(t) = p(t)$ and $s = +1$ (holes) or $c(t) = n(t)$ and $s = -1$ (electrons), $\mathbf{J}_\mathrm{c}$ is $\mathbf{J}_\mathrm{p}$ or $\mathbf{J}_\mathrm{n}$, $\mathbf{K}_\mathrm{c}$ is $\mathbf{K}_\mathrm{p}$ or $\mathbf{K}_\mathrm{n}$ and μ_c is μ_p or μ_n. The latter are taken here as scalars. Were it not for the second term at the left-hand side, (11) would be the usual DD expression for the current density. It is possible to perform easily a full inversion of the current density in terms of the DD current density $\mathbf{K}_\mathrm{c}^\mathrm{DD}(t)$

$$\mathbf{J}_\mathrm{c}(t) = \frac{1}{1 + \mu^2 B^2} \left(\mathbf{K}_\mathrm{c}^\mathrm{DD}(t) + s\mu\mathbf{K}_\mathrm{c}^\mathrm{DD}(t) \times \mathbf{B}(t) \right.$$
$$\left. + \mu^2 \left(\mathbf{K}_\mathrm{c}^\mathrm{DD}(t) \cdot \mathbf{B}(t)\right)\mathbf{B}(t)\right). \quad (13)$$

The parameter $|\mu B| \ll 1$ allows to write

$$\mathbf{J}_\mathrm{c}(t) = \mathbf{K}_\mathrm{c}^\mathrm{DD}(t) + s\mu_c\mathbf{K}_\mathrm{c}^\mathrm{DD}(t) \times \mathbf{B}(t). \quad (14)$$

[1]The symbol μ is used ubiquitously in the present paper, but its meaning is clear from the context.

The current-continuity equations and the Poisson equations complete the description of the drift-diffusion model, that is

$$\nabla \cdot \mathbf{J}_c(t) + sR(t) + s\partial_t c(t) = 0 \tag{15}$$

$$\nabla \left(-\epsilon \nabla V(t) \right) = \rho \left(V(t), \phi_p(t), \phi_n(t) \right). \tag{16}$$

Inside the metallic regions, the use of the approximation $|\mu_H B| \ll 1$ leads to the following expression for the current density

$$\mathbf{J}(t) = \sigma \mathbf{E}(t) + \mu_H \sigma \mathbf{E}(t) \times \mathbf{B}(t). \tag{17}$$

The current density satisfies the current-continuity equation $\nabla \cdot \mathbf{J} + \partial_t \rho = 0$. The magnetic field consists of two terms of which one represents the self-induced field and the other the external field $\mathbf{B}_{ext}$

$$\mathbf{B}(t) = \nabla \times \mathbf{A}(t) + \mathbf{B}_{ext}(t). \tag{18}$$

As can be seen from (5e), we now end up with a system of equations that should be solved self-consistently, i.e., $\mathbf{J}(t) = \mathbf{J}(V(t), \Pi(t), \mathbf{A}(t))$ since $\mathbf{A}(t) = \mathbf{A}(\Pi(t))$ and $\Pi(t) = \Pi(V(t), \mathbf{A}(t), \mathbf{J}(t))$. The self-consistency requirement sustains into the static regime as was already observed in [12].

IV. DISCRETIZATION OF THE LORENTZ CURRENT DENSITIES

In order to prepare the discretization process, we slightly modify (17) and cast it in the following form:

$$\begin{aligned} \mathbf{J}(t) &= \mathbf{J}^{EM}(t) + \mu_H \mathbf{J}^{EM} \times \mathbf{B}(t) \\ &= \mathbf{J}^{EM}(t) + \mathbf{J}^{LF}(t) \end{aligned} \tag{19}$$

$$\tag{20}$$

with

$$\begin{aligned} \mathbf{J}^{EM}(t) &= \sigma \mathbf{E}(t) \\ \mathbf{J}^{LF}(t) &= \mu_H \mathbf{J}^{EM}(t) \times \mathbf{B}(t). \end{aligned} \tag{21}$$

Equations (14), (17), and (19) show that the total current density consists of two contributions. The usual finite-integration method will lead to the nodal current-balance equations

$$\begin{aligned} \sum_j d_{ij} J_{ij}^{EM}(t) + \sum_j d_{ij} J_{ij}^{LF}(t) \\ + sR_i(t)\Delta v_i + s\partial_t c_i(t)\Delta v_i &= 0 \end{aligned} \tag{22}$$

where d_{ij} is the dual area and Δv_i is nodal volume of node i, and J_{ij}^{EM} represents the current-density expression as obtained without inclusion of the LF, e.g., for semiconductors it reads[2]

$$J_{c,ij}^{EM} = K_{c,ij}^{DD} = \frac{\mu_{c,ij}}{h_{ij}} \left(c_i B(sX_{ij}) - c_j B(-sX_{ij}) \right) \tag{23}$$

$$B(x) = \frac{x}{\exp(x) - 1}, \quad X_{ij} = \frac{q}{kT}(V_i - V_j + \text{sgn}_{ij}\Pi_{ij}) \tag{24}$$

$$\Pi_{ij} = \mathbf{e} \cdot \mathbf{\Pi}. \tag{25}$$

Here, $\mathbf{e}$ is an intrinsic unit vector along the direction of the grid link and $\text{sgn}_{ij} = +1$ if $\mathbf{e}$ points from node i to node

[2]We drop the explicit time dependence in the notation, but it is tacitly assumed.
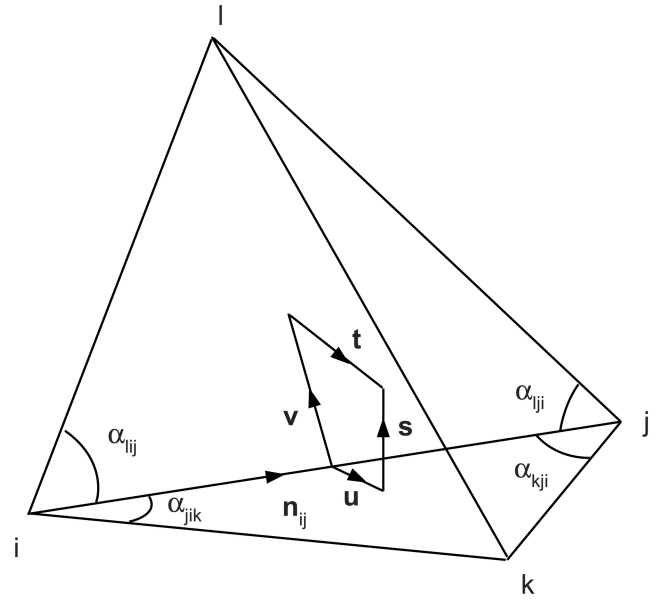

Fig. 1. Mesh element illustrating the ingredients of the decomposition of the LF vector product. Part of the dual area d_{ij} (see text) of the link $\langle ij \rangle$ is enclosed by the vectors $\mathbf{u}, \mathbf{v}, \mathbf{s}, \mathbf{t}$. The distance between node i and j is h_{ij}.

neighbor j. If $\mathbf{e}$ points from node j to node neighbor i, we have $\text{sgn}_{ij} = -1$. The variable h_{ij} is the length of the link. Furthermore, J_{ij}^{LF} represents the correction due to the Lorentz force, e.g. for semiconductors it is

$$J_{c,ij}^{LF}(t) = s\mu_c \left(\mathbf{K}_c^{DD}(t) \times \mathbf{B}(t) \right) \cdot \mathbf{n}_{ij}. \tag{26}$$

The vector $\mathbf{n}_{ij}$ is the unit vector along the link $\langle ij \rangle$ pointing from node i to node j and is parallel or antiparallel to $\mathbf{e}$. We will consider the discretization of (26). The current balance in each node is achieved by summing all contributions from each mesh element and its associated set of links that are attached to the node under consideration. In particular, a contributing link in some mesh element is a boundary segment of two adjacent faces in the element. The situation is illustrated in Fig. 1 for the link $\langle ij \rangle$ and the faces $F1 = \langle ijk \rangle$ and $F2 = \langle ijl \rangle$. Since we need the contribution of $\mathbf{K} \times \mathbf{B}$ in the direction $\langle ij \rangle$, we merely need the components of $\mathbf{K}$ and $\mathbf{B}$ in the plane of the dual area d_{ij}. The dual area of a link is defined as the surface element of the dual grid and is perpendicular to the link. All mesh cells of the primary grid that have the link as a boundary segment contribute to the dual area of the link. To compute $(\mathbf{K} \times \mathbf{B}) \cdot \mathbf{n}_{ij}$ we exploit two local coordinate frames in this plane; one coordinate frame $\{\mathbf{s}, \mathbf{t}\}$ is used to perform a decomposition of $\mathbf{B}$, and another coordinate frame $\{\mathbf{u}, \mathbf{v}\}$, whose base vectors are perpendicular to the first ones, is used to compute $\mathbf{K}$ in the volume segment spanned by the link $\langle ij \rangle$ and its dual area d_{ij} in the element. Using these two frames, we obtain that (Fig. 2)

$$\begin{aligned} \mathbf{K} \times \mathbf{B} &= (K_u \mathbf{u} + K_v \mathbf{v}) \times (B_s \mathbf{s} + B_t \mathbf{t}) \\ &= K_u B_s (\mathbf{u} \times \mathbf{s}) + K_v B_t (\mathbf{v} \times \mathbf{t}) \\ &\quad + K_u B_t (\mathbf{u} \times \mathbf{t}) + K_v B_s (\mathbf{v} \times \mathbf{s}). \end{aligned} \tag{27}$$

As can be seen from Fig. 2, the first two contribution will dominate the result whereas the last two terms vanish for
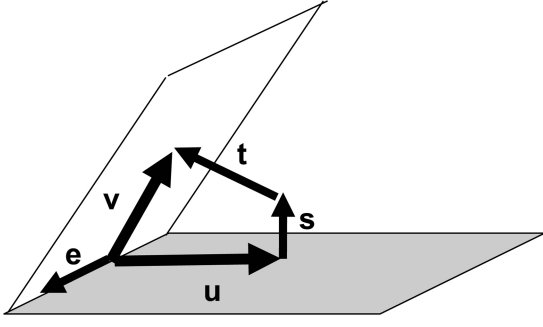
Fig. 2. Illustration of the decomposition of the LF vector product in the local coordinate bases.

orthogonal faces. For the last two terms, it is observed that their contribution seems maximal for acute angles between the adjacent faces, but then the dual area diminishes, resulting again in a small correction. Specifically, for the meshes that are used in this paper, the last two terms do not contribute. Therefore, we will implement the first two terms only which definitely suffices for structured grids and which will capture a large portion of the LF effects on unstructured grids [16]. The magnetic fields perpendicular to the primary grid surfaces $F1$ and $F2$, i.e., B_t and B_s, are obtained from the circulation of the vector potential along these surfaces. The self-induced magnetic field is given by

$$B_\perp = \frac{1}{\Delta S} \sum_k^N A_k h_k \qquad (28)$$

where $A_k \simeq \mathbf{A} \cdot \mathbf{e}_k$ and N is the number of links with lengths h_k around the surface and ΔS is the surface area. For completeness, we mention that the electric field is obtained in the finite-integration method from the voltage differences of the nodes of the discretization grid and the link variable representing the first-order time derivative of the vector potential as is seen in (24).

Finally, in order to obtain the variables K_u and K_v, a weighted sum is taken from the current-density projection along $\langle il \rangle$ and $\langle jl \rangle$ for K_u and in the same way for K_v, from $\langle ik \rangle$ and $\langle jk \rangle$. The weights include the angles α and the lengths of the sides of the surface. The details of the $\mathbf{K}$-calculation are found in (29)

$$
\begin{aligned}
K_u &= \frac{h_{ik}}{h_{ik} + h_{jk}} \sin(\alpha_{jik}) K_{ik} + \frac{h_{jk}}{h_{ik} + h_{jk}} \sin(\alpha_{ijk}) K_{jk} \\
K_v &= \frac{h_{il}}{h_{il} + h_{jl}} \sin(\alpha_{jil}) K_{il} + \frac{h_{jl}}{h_{il} + h_{jl}} \sin(\alpha_{ijl}) K_{jl}.
\end{aligned}
$$
(29)

The motivation for this procedure is found in the requirement that the final current density along the link $\langle ij \rangle$ should be antisymmetric in its indices, i.e., $K_{ji} = -K_{ij}$. This antisymmetry guarantees the aforementioned charge conservation. The Lorentz current is a vector and the magnetic induction is a pseudovector. Therefore, $\mathbf{K}$ needs to be a vector. It can be achieved by using the same K expressions when assembling the contribution to the link $\langle ij \rangle$ from the node i to the node j as when assembling the contribution to the link $\langle ji \rangle$ from

the node j to the node i. The requirement itself is needed to guarantee current balance. Let us now return to (26). Referring to (18), we observe that

$$\mathbf{K}(t) = \mathbf{K}(V(t), \phi^p(t), \phi^n(t), \mathbf{A}(t), \Pi(t), \mathbf{B}_{\text{ext}}(t)) \qquad (30)$$

and find that the Lorentz contribution to the total current depends only on the instantaneous time for which the current is evaluated. In other words, the LF does not generate terms containing explicit time derivatives. Remember that the time derivative of $\mathbf{A}$ is given by Π.

To compute the time derivatives of the degrees of freedom, we apply a BDF rule. In general, the BDF discretization performs the following substitution:

$$\frac{\partial f}{\partial t} = \frac{1}{h_0} \sum_{i=0} \alpha_{-i} f(t_{-i}). \qquad (31)$$

The parameters α depend on the time step sizes, and t_0 corresponds to the latest time instance. Our implementation is limited to the second-order BDF. In this case, we have

$$
\begin{aligned}
\alpha_{-1} &= -\frac{t_0 - t_{-2}}{t_{-1} - t_{-2}}. \\
\alpha_{-2} &= -\frac{t_0 - t_{-1}}{t_0 - t_2} \times \frac{t_0 - t_{-1}}{t_{-2} - t - 1}. \\
\alpha_{-0} &= -\alpha_{-1} - \alpha_{-2}.
\end{aligned}
$$
(32)

For equal time step sizes, the values are $\alpha_{-1} = -2$, $\alpha_{-2} = \frac{1}{2}$, and $\alpha_0 = \frac{3}{2}$, respectively.

We have now all ingredients available to build the discretized equations. Using the implicit BDF scheme, the solution at the latest time instance is found by applying a Newton–Raphson solver to the full set of equations. The degrees of freedom are the temporal nodal variables $V_i(t)$, $\phi_i^p(t)$, and $\phi_i^n(t)$ and the link variables $A_i(t)$ and $\Pi_i(t)$. If we denote the Poisson equation or the current-continuity equation in metallic domains, i.e., (5a) as $\mathcal{P}(V, \phi^p, \phi^n, \Pi, A) = 0$, the hole current continuity (5c) as $\mathcal{J}^p(V, \phi^p, \phi^n, \Pi, A) = 0$, the electron current continuity (5b) as $\mathcal{J}^n(V, \phi^p, \phi^n, \Pi, A) = 0$, the Maxwell–Ampere equation (5e) as $\mathcal{M}(V, \phi^p, \phi^n, \Pi, A) = 0$ and the Π defining relation (5d) as $\mathcal{Q}(A) = 0$, then the Newton–Raphson updates ΔV, $\Delta \phi^p$, $\Delta \phi^n$, $\Delta \Pi$, ΔA are computed from the following linear system:

$$
\begin{bmatrix}
\frac{\partial \mathcal{P}}{\partial V} & \frac{\partial \mathcal{P}}{\partial \phi^p} & \frac{\partial \mathcal{P}}{\partial \phi^n} & \frac{\partial \mathcal{P}}{\partial \Pi} & \frac{\partial \mathcal{P}}{\partial A} \\
\frac{\partial \mathcal{J}^p}{\partial V} & \frac{\partial \mathcal{J}^p}{\partial \phi^p} & \frac{\partial \mathcal{J}^p}{\partial \phi^n} & \frac{\partial \mathcal{J}^p}{\partial \Pi} & \frac{\partial \mathcal{J}^p}{\partial A} \\
\frac{\partial \mathcal{J}^n}{\partial V} & \frac{\partial \mathcal{J}^n}{\partial \phi^p} & \frac{\partial \mathcal{J}^n}{\partial \phi^n} & \frac{\partial \mathcal{J}^n}{\partial \Pi} & \frac{\partial \mathcal{J}^n}{\partial A} \\
\frac{\partial \mathcal{M}}{\partial V} & \frac{\partial \mathcal{M}}{\partial \phi^p} & \frac{\partial \mathcal{M}}{\partial \phi^n} & \frac{\partial \mathcal{M}}{\partial \Pi} & \frac{\partial \mathcal{M}}{\partial A} \\
\frac{\partial \mathcal{Q}}{\partial V} & \frac{\partial \mathcal{Q}}{\partial \phi^p} & \frac{\partial \mathcal{Q}}{\partial \phi^n} & \frac{\partial \mathcal{Q}}{\partial \Pi} & \frac{\partial \mathcal{Q}}{\partial A}
\end{bmatrix}
\cdot
\begin{bmatrix}
\Delta V \\
\Delta \phi^p \\
\Delta \phi^n \\
\Delta \Pi \\
\Delta A
\end{bmatrix}
= -
\begin{bmatrix}
\mathcal{P} \\
\mathcal{J}^p \\
\mathcal{J}^n \\
\mathcal{M} \\
\mathcal{Q}
\end{bmatrix}.
$$

The fragments $\frac{\partial \mathcal{P}}{\partial A}$, $\frac{\partial \mathcal{J}^p}{\partial A}$, and $\frac{\partial \mathcal{J}^n}{\partial A}$ are induced by the LF whereas other parts get additional contributions from the LF. Furthermore, we note that $\frac{\partial \mathcal{Q}}{\partial V} = \frac{\partial \mathcal{Q}}{\partial \phi^p} = \frac{\partial \mathcal{Q}}{\partial \phi^n} = 0$. Another interesting observation is that $\frac{\partial \mathcal{Q}}{\partial \Pi}$ and $\frac{\partial \mathcal{Q}}{\partial A}$ are diagonal matrices. Therefore, it is straightforward to solve for ΔA in terms of $\Delta \Pi$. The solution is

$$\Delta A = -\left(\frac{\partial \mathcal{Q}}{\partial A}\right)^{-1} \left[\mathcal{Q} + \frac{\partial \mathcal{Q}}{\partial \Pi} \Delta \Pi \right]. \qquad (33)$$
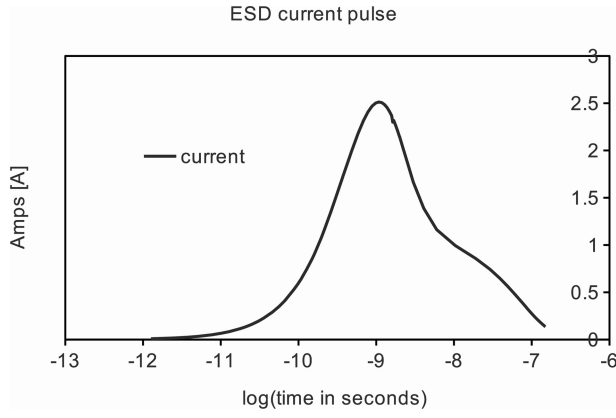
Fig. 3. Typical ESD current pulse used in the simulation of the fast-transient signals.
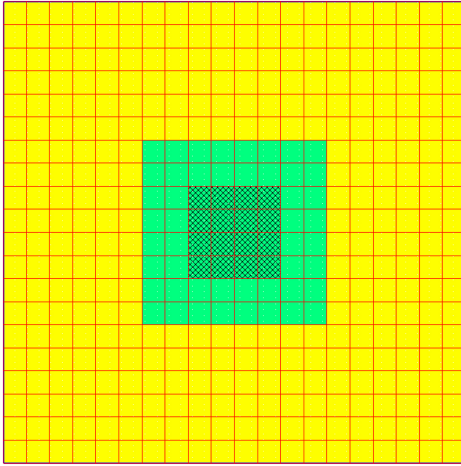

Fig. 4. 2-D cross section of the silicon wire.

In this way, we can eliminate the last column of the matrix system

$$
\begin{bmatrix}
\frac{\partial \mathcal{P}}{\partial V} & \frac{\partial \mathcal{P}}{\partial \phi^p} & \frac{\partial \mathcal{P}}{\partial \phi^n} & \frac{\partial \mathcal{P}}{\partial \Pi} - \frac{\partial \mathcal{P}}{\partial A}\left(\frac{\partial \mathcal{Q}}{\partial A}\right)^{-1}\frac{\partial \mathcal{Q}}{\partial \Pi} \\
\frac{\partial \mathcal{J}^p}{\partial V} & \frac{\partial \mathcal{J}^p}{\partial \phi^p} & \frac{\partial \mathcal{J}^p}{\partial \phi^n} & \frac{\partial \mathcal{J}^p}{\partial \Pi} - \frac{\partial \mathcal{J}^p}{\partial A}\left(\frac{\partial \mathcal{Q}}{\partial A}\right)^{-1}\frac{\partial \mathcal{Q}}{\partial \Pi} \\
\frac{\partial \mathcal{J}^n}{\partial V} & \frac{\partial \mathcal{J}^n}{\partial \phi^p} & \frac{\partial \mathcal{J}^n}{\partial \phi^n} & \frac{\partial \mathcal{J}^n}{\partial \Pi} - \frac{\partial \mathcal{J}^n}{\partial A}\left(\frac{\partial \mathcal{Q}}{\partial A}\right)^{-1}\frac{\partial \mathcal{Q}}{\partial \Pi} \\
\frac{\partial \mathcal{M}}{\partial V} & \frac{\partial \mathcal{M}}{\partial \phi^p} & \frac{\partial \mathcal{M}}{\partial \phi^n} & \frac{\partial \mathcal{M}}{\partial \Pi} - \frac{\partial \mathcal{M}}{\partial A}\left(\frac{\partial \mathcal{Q}}{\partial A}\right)^{-1}\frac{\partial \mathcal{Q}}{\partial \Pi}
\end{bmatrix}
\cdot
\begin{bmatrix}
\Delta V \\ \Delta \phi^p \\ \Delta \phi^n \\ \Delta \Pi
\end{bmatrix}
$$

$$
=
\begin{bmatrix}
-\mathcal{P} + \frac{\partial \mathcal{P}}{\partial A}\left(\frac{\partial \mathcal{Q}}{\partial A}\right)^{-1}\mathcal{Q} \\
-\mathcal{J}^p + \frac{\partial \mathcal{J}^p}{\partial A}\left(\frac{\partial \mathcal{Q}}{\partial A}\right)^{-1}\mathcal{Q} \\
-\mathcal{J}^n + \frac{\partial \mathcal{J}^n}{\partial A}\left(\frac{\partial \mathcal{Q}}{\partial A}\right)^{-1}\mathcal{Q} \\
-\mathcal{M} + \frac{\partial \mathcal{M}}{\partial A}\left(\frac{\partial \mathcal{Q}}{\partial A}\right)^{-1}\mathcal{Q}
\end{bmatrix} .
$$

We found that a submission of the matrix system without using this elimination to the indirect solver combo consisting of reordering, preconditioning, and linear solving soon led to too much fill-in due to the fact that $\frac{\partial \mathcal{Q}}{\partial A}$ and $\frac{\partial \mathcal{Q}}{\partial \Pi}$ are of the same numerical size. Therefore, there will be a complete fill-in triggered in the lower right corner of the matrix. Remember that the corresponding size is of the order of the number of links and is three times the order of number of nodes. As a consequence, even such a partial fill-in is deteriorating the solving process. However, there are no issues anymore with
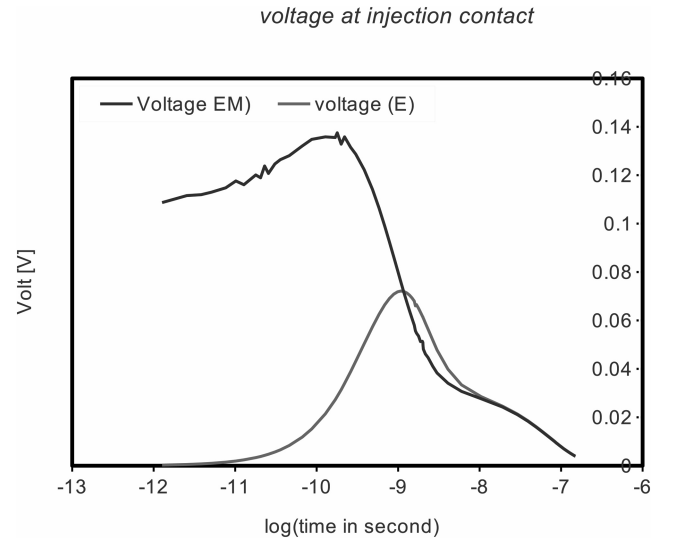
voltage at injection contact

Fig. 5. ESD voltage pulse computed in the simulation of the fast-transient signals at the injection contact.
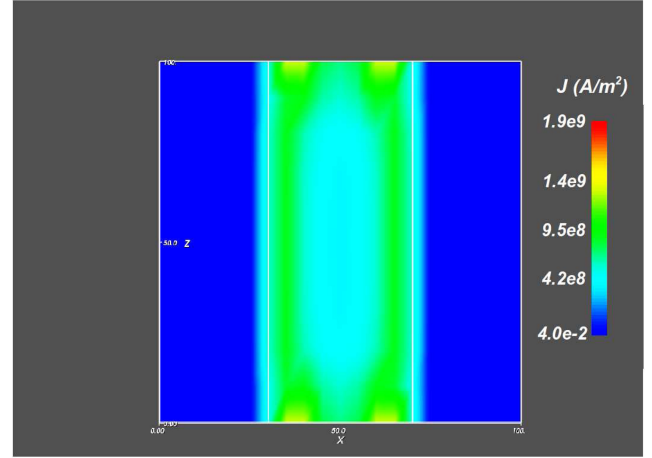

Fig. 6. Current density at 0.30×10^{-9} sec. Some reduction is observed in the center due to the skin effect.

fill-in at the preconditioning stage for the second version of the matrix system. As a postprocessing step after solving we apply (33) for obtaining the update on the vector potential.

Another interesting observation is that the complete non-linear system of equations, i.e., $\mathbf{F}(\mathbf{X}) = 0$, where $\mathbf{X} = \{V, \phi^p, \phi^n, \Pi, \mathbf{A}\}$ can be reformulated as

$$ \mathbf{F}_0(\mathbf{X}) + \Delta \mathbf{F}(\mathbf{X}) = 0 . \tag{34} $$

Here, $\mathbf{F}_0(\mathbf{X})$ consists of all terms that do not contain any reference to the LF while $\Delta \mathbf{F}(\mathbf{X})$ refers exclusively to terms induced by the LF. An iterative solution method can be realized that simplifies the Newton–Raphson matrix substantially. The pseudocode reads as follows:

1) *compute the initial guess* $\mathbf{X} = \mathbf{X}_0$ *using* $\mathbf{F}_0(\mathbf{X}) = 0$;
2) *while* $|\mathbf{X}_{n+1} - \mathbf{X}_n| \geq \epsilon$ *solve* $\mathbf{X}_{n+1}$ *using* $\mathbf{F}_0(\mathbf{X}_{n+1}) = -\Delta \mathbf{F}(\mathbf{X}_n)$.

An alternative approach performs the full Newton–Raphson matrix assembling but computes an intermediate solution based on the following pseudo code:
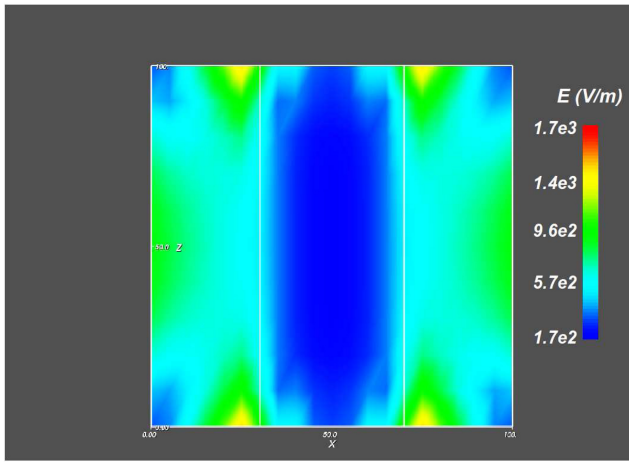
Fig. 7. Electric field intensity at 0.30×10^{-9} s. Some reduction in the center is observed due to skin effect and the value is $\sim 10^3$ V/m.
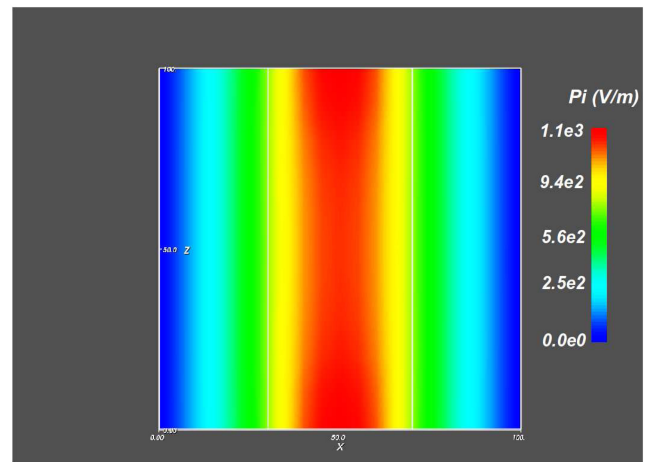

Fig. 9. Magnitude of the pseudocanonical momentum $\Pi = \partial_t \mathbf{A}$ at 0.30×10^{-9}. The maximum value is $\sim 10^3$ V/m.
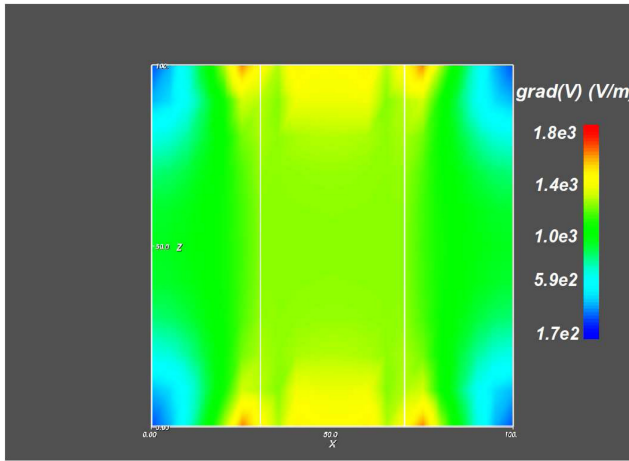

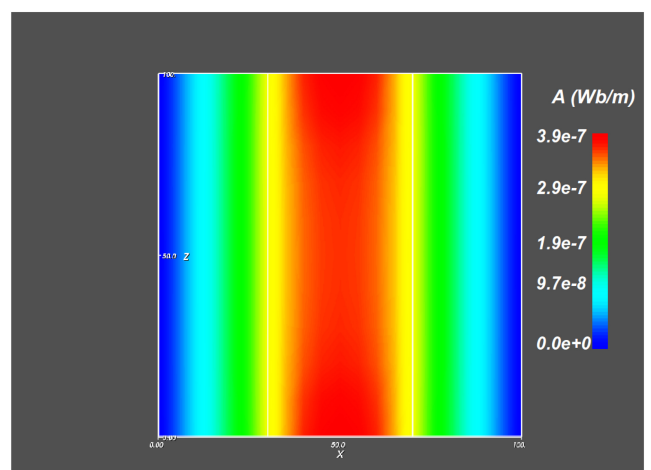Fig. 8. Magnitude of ∇V at 0.30×10^{-9} s. The maximum value is $\sim 10^3$ V/m.

Fig. 10. Magnitude of the vector potential $\mathbf{A}$ at 0.30×10^{-9} sec. The maximum value is $3 \sim \times 10^{-7}$ Vsec/m.

1) *compute an initial guess* $\mathbf{X} = \mathbf{X}_0$ *using* $\mathbf{F}_0(\mathbf{X}) = 0$;
2) *compute an update* $\Delta \mathbf{X}$ *from* $\frac{\partial \mathbf{F}}{\partial \mathbf{X}}|_{\mathbf{X}_0} \cdot \Delta \mathbf{X} = -\Delta \mathbf{F}$;
3) *solve* $\mathbf{F}(\mathbf{X}) = 0$ *using* $\mathbf{X}_0 + \Delta \mathbf{X}$ *as initial guess.*

V. APPLICATIONS

A. Silicon Wire

Continuing with the example that was given in [12], we first consider a silicon wire. The purpose is to demonstrate the convergence behavior of the solution scheme that is proposed in this paper and to obtain a first impression of the size of the modifications induced by the magnetic field effects as well as the LF in the transient regime. In Fig. 3, a typical ESD current pulse is shown. The spike of the currents ramps up within a nanosecond. We consider a silicon wire with a square cross section of 40 x 40 μm^2. Contacts with areas of size 20 x 20 μm^2 are placed at the ends. A structured grid is used in this example although not essential. A 2-D cross section of the wire that is embedded in a 100 x 100 μm^2 block of oxide is shown in Fig. 4. The wire length is 100 μm. The doping of the silicon wire (N-type) is 10^{20} cm^{-3}. We apply a current boundary condition at one contact and a voltage boundary condition ($V = 0$) at the other end contact of the wire. The calculations are performed on a mesh of 4851 nodes. Since a current boundary condition is applied at the current injection contact, the contact voltage is computed. The result is shown in Fig. 5. The two curves correspond to simulations with the magnetic field components switched on (curve EM) and with the magnetic field switched off (curve E). As can be seen, there is a large difference at the ramp-up stage. This can be understood as follows: In order to push the current through the silicon wire an applied voltage must be set. Due to the induced electric field, this counteracts the applied field, and a higher voltage must be applied. This is confirmed in the various plots of the field components. Fig. 6 shows the current density in the silicon wire at the time instance 0.30×10^{-9} s, Figs. 7–9 show the electric field intensity, the contribution ∇V to the electric field, and the induced contribution Π to this field. Both contributions are roughly equal in magnitude. For completeness, we also show the magnitude of the vector potential, A in Fig. 10. The peak value is $\sim 10^{-7}$ Wb/m. Finally, Fig. 11 shows the magnetic induction. All field plots are taken at 0.30×10^{-9} sec. At this time instance, the fast-transient phenomena are very pronounced. Finally, Fig. 12
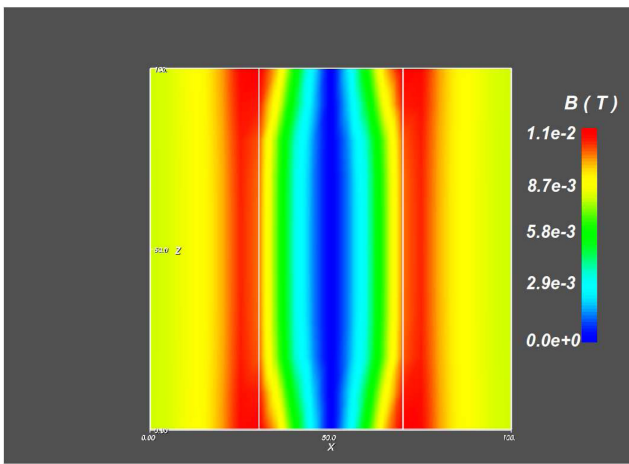
Fig. 11. Magnitude of the magnetic induction, **B** at 0.30×10^{-9} sec. The maximum value is $\sim 10^{-2}$ T.
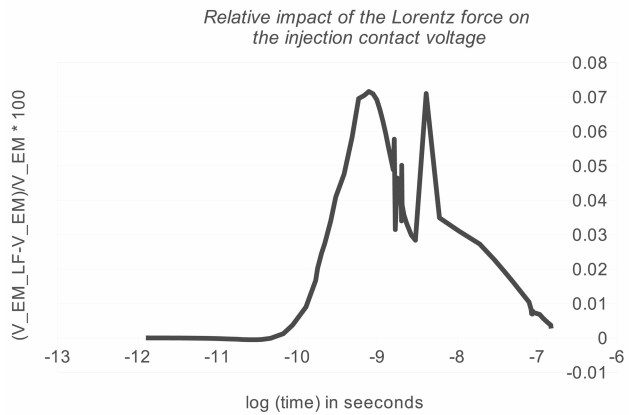

Fig. 12. Relative change in the voltage of the current injection contact due to the Lorentz force.
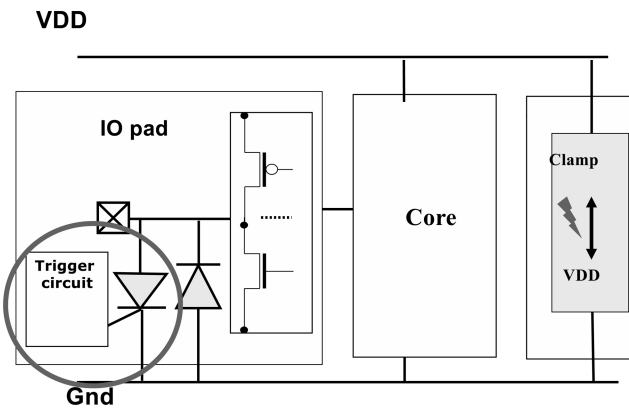

Fig. 13. Circuit layout for use of a Silicon-Controlled Rectifier (SCR). The location of the SCR is encircled and is presented in more detail in Fig. 14.

gives the relative change in the voltage of the current-injection contact. The peak value is $\sim 0.07\%$, which is more or less inline with the observations for the static case [12]. All results were obtained with a relative current balance being of the order of $\sim 0.0001\%$. This accuracy is sufficiently high in order to detect the impacts of the various mechanisms.
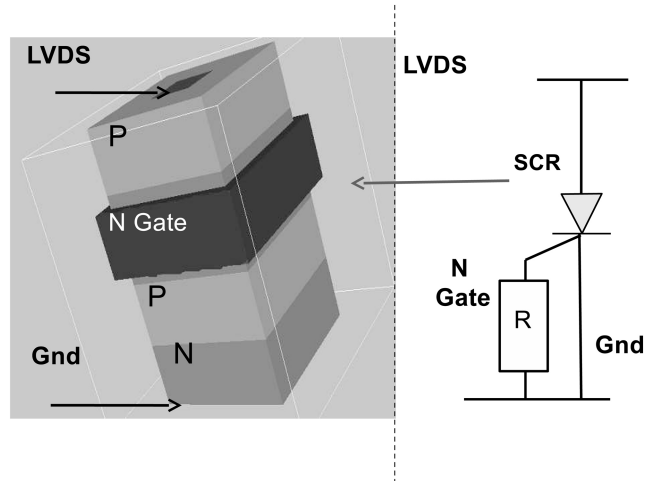

Fig. 14. Device implementation the SCR. The left picture is a stretched view of the actual implementation that is presented in Fig. 15.
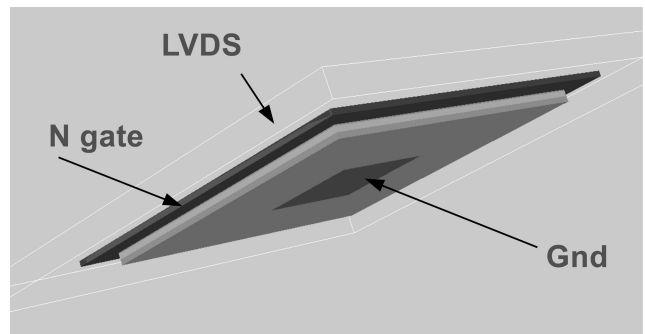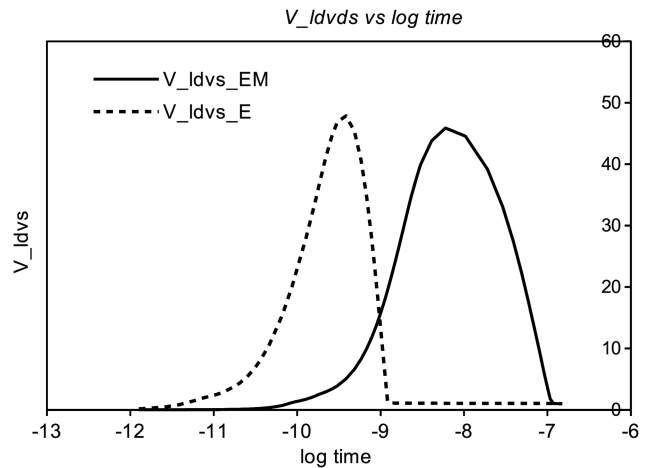

Fig. 15. Actual implementation of the SCR structure.

Fig. 16. Change in the voltage of the current injection contact due to magnetic effects.

B. ESD Protection

A second illustration deals with a stacked diode pair that serves as a prototype for a circuit topology corresponding to an ESD protection structure [17]. The circuit lay-out is found in Fig. 13 and a physical realization is shown in Figs. 14 and 15. The latter shows a stretched view of the silicon-controlled rectifier (SCR) by stacking N-doped and P-doped regions. The N-gate contact, the third layer counted from
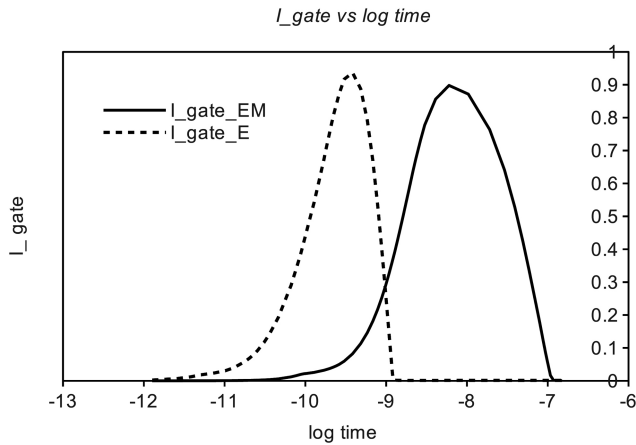
Fig. 17. Change in the gate current due to magnetic effects.

Fig. 19. Change in the voltage of the current injection contact (LVDS, dashed line) and change in the gate current (continuous line) due to an additional switch-on of the Lorentz force for the minority carriers.
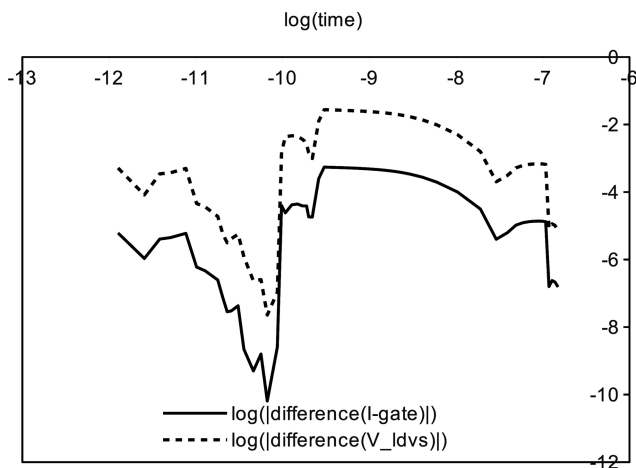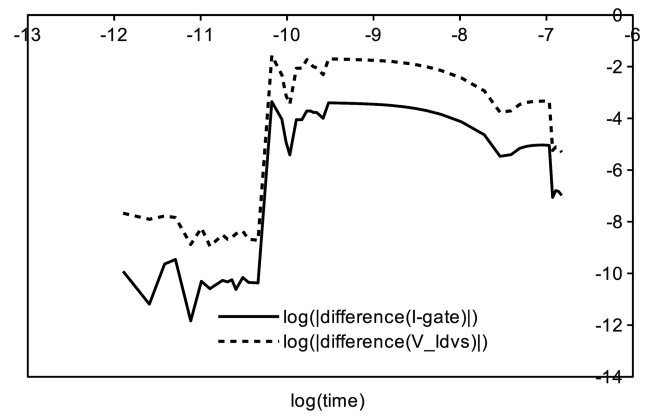

Fig. 18. Change in the gate current and change in the voltage of the current injection contact (LVDS) due to switch-on of the Lorentz force for the majority carriers.
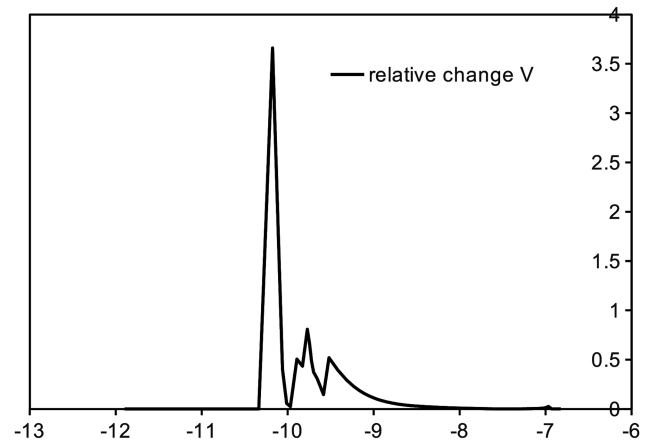

Fig. 20. Relative change in the voltage of the current injection contact (LVDS) due to an additional switch-on of the Lorentz force for the minority carriers.

below, is surrounded by a metallic ring at which the gate contact is placed with a load of 50 Ω. The current is as given in Fig. 3 and is injected through the top contact LVDS. A ground contact (Gnd) is inserted at the bottom of the stack.

The results of the simulation of the voltage at the LVDS contact are found in Fig. 16. The effect of the magnetic field on the gate current is shown in Fig. 17. Both results clearly illustrate that the electromagnetic response has an important effect. There is a significant signal delay more than a change in amplitude of the signals. Finally, we consider the inclusion of the LF in the calculation. This is done in two stages. First, we switch on the LF corrections for the majority carriers, i.e., in the N-doped regions, the LF effect is included for electrons, whereas in P-doped regions it is included for holes. At a second stage, we include the LF for both types of carriers in both types of doped regions. In Fig. 18, the impact of the majority-carrier inclusion on the results is shown. The dashed line shows the comparison of the voltage value at the current injection with and without inclusion of LF, whereas the continuous line shows the comparison for the gate current. In order to see the impact of the LF for minority carriers, we compare the results of the calculation with inclusion of the majority-carrier Lorentz-force with the results obtained by

switching on all terms, i.e., the LF correction is applied to both majorities and majorities. Fig. 19 shows the difference of the voltage value at the current injection (dashed line), and the difference for the gate current (continuous line) with and /without inclusion of the minority-carrier LF term. As seen in Fig. 19, the minority carriers induce a change of the injection voltage value of approximately 1.82 V, which corresponds to a relative change of 3.5% as seen in Fig. 20.

VI. CONCLUSION

We presented a full simulation picture of fast-transient phenomena. Besides the electromagnetic effects, we provided a method to compute the impact of the LF. We applied the proposed method to a silicon wire. Furthermore, we applied the method to a simplified implementation of a SCR that serves as a local protection structure for forward stress. There is convincing evidence that the magnetic contributions are of the same order of magnitude as the electric contributions. On the other hand, the LF effects are very minor and can be ignored for most practical purposes (despite the fact that it is an arduous task to compute these effects). In the fast-transient applications that we have done, their impact is of the order of $\sim 0.07\%$ in normal operation but minorities subjected

to the LF and fast-transient conditions lead to an appreciable deviation ($\sim$ 3%) for the voltage values that are needed to realize the large transient currents. The proposed method for calculating the LF induced modifications may be applied to other fields of engineering and physics in which the LF plays a more dominant role. For example, the numerical scheme can be applied to simulate Hall sensors.

VII. ACKNOWLEDGMENT

REFERENCES

[1] G. F. Wang, R. W. Dutton, and C. S. Rafferty, "Device-level simulation of wave propagation along metal-insulator-semiconductor interconnects," *IEEE Trans. Microwave Theory Tech.*, vol. 50, no. 4, pp. 1127–1136, Apr. 2002.

[2] F. Bertazzi, F. Cappelluti, S. D. Guerrieri, F. Bonani, and G. Ghione, "Self-consistent coupled carrier transport full-wave EM analysis of semiconductor traveling-wave devices," *IEEE Trans. Microwave Theory Tech.*, vol. 54, no. 4, pp. 1611–1617, Apr. 2006.

[3] K. J. Willis, S. C. Hagness, and I. Knezevic, "Multiphysics simulation of high-frequency carrier dynamics in conductive materials," *J. Appl. Phys.*, vol. 10, no. 6, pp. 063 714.1–063 714.15, Sep. 2011.

[4] P. Meuris, W. Schoenmaker, and W. Magnus, "Strategy for electromagnetic interconnect modeling," *IEEE Trans. Comput. Aided Design*, vol. 20, no. 6, pp. 753–762, Jun. 2001.

[5] W. Schoenmaker and P. Meuris, "Electromagnetic interconnects and passives modeling: Software implementation issues," *IEEE Trans. Comput. Aided Design*, vol. 21, no. 5, pp. 534–543, May 2002.

[6] K. Lipnikov, G. Manzini, F. Brezzi, and A. Buffa, "The mimetic finite difference method for the 3D magnetostatic field problems on polyhedral meshes," *J. Comput. Phys.*, vol. 20, no. 5, pp. 305–328, Jan. 2011.

[7] T. Weiland, "Time domain electromagnetic field computation with finite difference methods," *Int. J. Numer. Model. Electron. Netw., Devices Fields*, vol. 9, pp. 295–319, Jul. 1996.

[8] E. Noether, "Invariante variationsprobleme," *Nachr. D. König. Gesellsch. D. Wiss. Zu Göttingen, Math-phys. Klasse*, pp. 235–257, 1918.

[9] W. Schoenmaker, M. Matthes, B. D. Smedt, S. Baumanns, C. Tischendorf, and R. Janssen, "Large signal simulation of integrated inductors on semi-conducting substrates," in *Proc. DATE*, Mar. 2012, pp. 1221–1226.

[10] Q. Chen, W. Schoenmaker, G. Chen, L. Jiang, and N. Wong, "A numerically efficient formulation for time-domain electromagnetic-semiconductor cosimulation for fast transient systems," *IEEE Trans. Comput. Aided Design*, vol. 32, no. 5, pp. 802–806, May 2013.

[11] W. Schoenmaker, P. Meuris, P. Galy, and J. Jiminez, "On the inclusion of lorentz force effects in TCAD simulations," in *Proc. ESSDERC*, Sep. 2010, pp. 190–193.

[12] W. Schoenmaker, P. Meuris, J. Jiminez, and P. Galy, "On the inclusion of Lorentz force effects in TCAD simulations," *Solid State Electron.*, vols. 65–66, pp. 103–107, Dec. 2011.

[13] Q. Chen, W. Schoenmaker, P. Meuris, and N. Wong, "An effective formulation of coupled electromagnetic-TCAD simulation for extremely high frequency onwards," *IEEE Trans. Comput. Aided Design*, vol. 30, no. 6, pp. 866–876, Jun. 2011.

[14] S. Laux and K. Hess, "Rivisiting the analytic theory of p-n junction impedance: Improvements guided by computer simulation leading to a new equivalent curcuit," *IEEE Trans. Electron Devices*, vol. 46, no. 2, pp. 396–412, Feb. 1999.

[15] M. Rudan, S. Reggiani, E. Gnani, G. Baccarani, C. Corvasce, D. Barlini *et al.*, "Theory and experimental validation of a new analytical model for the position-dependent hall voltage in devices with arbitrary aspect ratio," *IEEE Trans. Electron Devices*, vol. 53, no. 2, pp. 314–322, Feb. 2006.

[16] W. Schoenmaker, P. Meuris, E. Janssens, W. Schilders, and D. Ioan, "Modeling of passive-active device interactions," in *Proc. ESSDERC*, Sep. 2007, pp. 163–166.

[17] P. Galy, J. Jimenez, W. Schoenmaker, P. Meuris, and O. Dupuis, "ESD RF protections in advanced CMOS technologies and its parasitic capacitance evaluation," in *Proc. ICICDT*, May. 2011, pp. 1–4.

Wim Schoenmaker received the B.Sc. and M.Sc. degrees in theoretical physics from the Free University of Amsterdam, Amsterdam, The Netherlands, in 1975 and 1979, respectively, and the Ph.D. degree in theoretical high-energy physics from the University of Groningen, Groningen, The Netherlands, in 1983.

From 1983 to 1987, he was a Post-Doctoral Fellow with the University of Kaiserslautern, Kaiserslautern, Germany, and the University of Leuven, Leuven, Belgium. From 1987 to 2003, he was with IMEC, Leuven, where he has been involved in the development of numerical simulation tools and computer-aided design (CAD) tools for the study and design of electronic devices at the submicrometer level. From 1993 to 2003, he led the Technology CAD Group at IMEC. He is the co-founder and the CTO of the company MAGWEL. His current research interests include lattice gauge theories, statistical physics, and computing.

From 1998 to 2005, he was an Associate Editor of the IEEE TRANSACTIONS ON COMPUTER-AIDED DESIGN.

Quan Chen (S'09–M'11) received the B.S. degree in electrical engineering from the Sun Yat-Sen University, China, in 2005, and the M.Phil. and Ph.D. degrees in electronic engineering from the University of Hong Kong, Kowloon, Hong Kong, in 2007 and 2010, respectively.

From 2010 to 2011, he was a Post-Doctoral Fellow with the Department of Computer Science and Engineering, University of California, San Diego, CA, USA. He is currently a Research Assistant Professor with the Department of Electrical and Electronics Engineering, University of Hong Kong. His current research interests include multiphysics modeling, simulation of microelectronics, and large scale scientific computation.

Philippe Galy received the Ph.D. and H.D.R. (academic research supervisor) from University of Bordeaux. He is a Senior Expert in micro and nano-electronics with STMicrolectronics Research and Development, Crolles, France.

He proposed a full CDM protection strategy validated by silicon proof. He has proposed several new ESD compact devices with associated trigger circuits for ESD networks. He leads several groups in IP infrastructure teams for research and development focused on transistor levels to the SoC levels for robust IP integration. Prior to that, he was a Professor with the Leonard de Vinci Enigineering School in Paris for ten years. He has authored or coauthored several publications, books, and patents.

His current research interests include SCR, T2, BIMOS transistor, Beta-structure, and other innovative devices.

Dr. Galy serves in TPC and is a Reviewer for many symposiums and for TED/SSE.